Optical characterization of Er-implanted Y_2O_3 waveguide films

Erik Radius

Supervisors: Drs. G.N. van den Hoven, Drs. E. Snoeks, Dr. A. Polman

FOM Institute for Atomic and Molecular Physics, Kruislaan 407

1098 SJ Amsterdam, the Netherlands

Verslag van de Eigen Werk IV stage voor de afstudeerrichting Experimentele Natuurkunde

aan de faculteit Natuur- en Sterrenkunde van de Universiteit van Amsterdam

8 augustus 1993 - 26 juni 1994

Contents

1. Preface

Telecommunication technology has discovered light. Optical fibers allow for data transport at a high speed and a huge bandwidth. Taking full advantage of the optical superhighway requires the development of optical computers and integration of electronical and optical processes on one device, a chip. This field of electro-optics forms a challenge for both fundamental and applied research.

In these days, the applicability of planar optical devices and waveguides of integrated circuit-like dimensions is still limited, partly due to considerable optical losses (e.g. in splitters, coupling losses, etcetera). Doping of the devices with optically active ions can play an important role in obtaining a zero-loss device or an optical amplifier on the chip. A very suitable dopant is the rare earth Er which, when incorporated in a host material in the trivalent (Er^{3+}) state, can luminesce at a wavelength of 1.53 μm. These 1.5 μm transitions coincide with a standard telecommunication window, which corresponds to an absorption minimum of silica fibers in the wavelength range of 1.5 to 1.6 μm. All rare earth ions in the trivalent state have filled 5s and 5p shells around a partially filled 4f shell. These filled shells reduce the influence of the host material on the rare earth ions. For the Er^{3+} ion this gives rise to sharp optical transitions between the 4f levels and long lifetimes of typically several milliseconds of the metastable (first excited) state. A long lifetime of the metastable state is essential for an efficient laser or optical amplifier.

In this work, Er-doping is performed in thin Y_2O_3 films on an oxidized Si substrate. Advantages of using Y_2O_3 as a host material for Er include

- the low optical loss in the near infrared and low phonon energy of Y_2O_3.
- the expected high solubility of Er in Y_2O_3 when comparing the Er_2O_3 and Y_2O_3 lattice (crystal structure Ia3, lattice constant a_0 resp. 10.547 Å and 10.604 Å) and the ion radii of Y (0.893 Å) and Er (0.881 Å).[1]

A convenient means of incorporating Er ions in thin films is ion implantation, an extensively used technique in semiconductor research and industry. Advantages of optical doping by ion implantation include the Gaussian shape of the implantation profile — well-suited for matching to an optical mode in a waveguide. However, the high Er concentrations needed in short planar amplifiers are known to deteriorate the luminescence efficiency at 1.53 μm due to Er-Er interactions. In this work, photoluminescence properties of Y_2O_3 implanted with Er to a peak concentration of 0.75 at%, excited with a high-intensity 1480 nm laser beam were investigated. Er luminescence was observed at wavelengths ranging from near-IR to near-UV, attributed to transitions to the ground state from higher energy levels than the pump band. Decay measurements show remarkably long lifetimes of several energy levels. Two mechanisms known to populate higher energy levels than the pump band, namely excited state absorption and cooperative upconversion, were used to explain the obtained data. Next to the luminescence study, this report contains a technical description of the experimental setup which was designed and built for stable in-plane coupling of intense laser light into thin planar structures. The key components are discussed in Appendix A and a laser to fiber coupling manual is supplied in Appendix B.

2. Experimental

2.1 Y_2O_3 thin film fabrication

An Y_2O_3 film was prepared by reactive sputter deposition[2] on a substrate consisting of a Si {100} wafer with a thermally oxidised, 3 μm thick bufferlayer of SiO_2. Sputter deposition was performed in a 90% Ar, 10% O_2 atmosphere (sputter chamber pressure 7×10^{-4} mbar) using a magnetron sputtergun containing a solid Y target. The substrate temperature was 200 °C. The resulting structure of the Y_2O_3 is a cubic polycrystalline phase and the film has a nominal thickness of 0.59 μm. Preparation of the film was carried out at the university of Twente (Dr. T.H. Hoekstra, Dr. P.V. Lambeck).

2.2 Ion Implantation of Er into Y_2O_3 films

Ion implantation of Er was performed with a single-ended 1 MV Van de Graaff-type accelerator.[3] A sputter ion source containing a solid Er target produced an ion beam which, after mass-selection in a Wien filter, was accelerated to 800 keV. The projected range at this energy is 136 ± 30 nm.[4] After energy selection in an analysing magnet the ion beam was focused onto a diaphragm and electrostatically scanned over the $Y_2O_3/SiO_2/Si$ sample surface. The beam current on target was 3μA. The samples were kept at room temperature. The implantation fluence was 1×10^{16} ions/cm^2. The samples received a post-implantation thermal anneal treatment at a temperature of 700 °C in a quartz vacuum furnace ($p < 10^{-6}$ mbar) for 1 hour.

2.3 Rutherford Backscattering Spectroscopy

Using Rutherford Backscattering Spectroscopy (RBS), one can obtain precise information on the presence of atomic species and their concentration as a function of depth. RBS analysis was performed with a single-ended 2 MV Van de Graaff-type accelerator. An rf-type ion source produced a beam of Heparticles which was accelerated to 2 MeV. After energy selection in an analyzing magnet the beam passed collimation optics and impinged on the sample. Backscattered He particles were detected at a backscattering angle of 169° using a standard Si surface barrier detector cooled to 0 °C. Spectral analysis and simulations were performed with the RBS simulation program RUMP.[5]

Figure 1 shows an RBS spectrum of the Er-implanted Y_2O_3 film on thermally oxidised Si. The Y, O and Er surface channels are indicated. The dotted lines indicate the SiO_2 substrate. From the width of the Y ridge and the theoretical density of bulk Y_2O_3 ($\rho = 5.01$ g/cm^3), the thickness of the Y_2O_3 layer is determined to be 0.49 μm.

The Er implantation profile has a Gaussian shape, peaking at a depth of 0.14 μm with a full width at half maximum (FWHM) of 0.10 μm. The Er profile is superimposed on a small background signal from a Ta contamination in the film. This prevents an accurate determination of the Er dose, moreover, part of the Er profile coincides with the Y signal. A simultaneous implant of Er into Al_2O_3 was performed for Er dose

determination: RBS analysis (not shown) of this sample show that an Er dose of 9.8×10^{15} ions/cm^2 was present. The Er peak concentration in the Y_2O_3 film was around 0.75 at%.

RBS analysis (not shown) of an unimplanted sample shows a 0.15 at% Ta and 0.7 at% Ar contamination throughout the deposited Y_2O_3 layer, both of which can be attributed to the sputter deposition conditions.

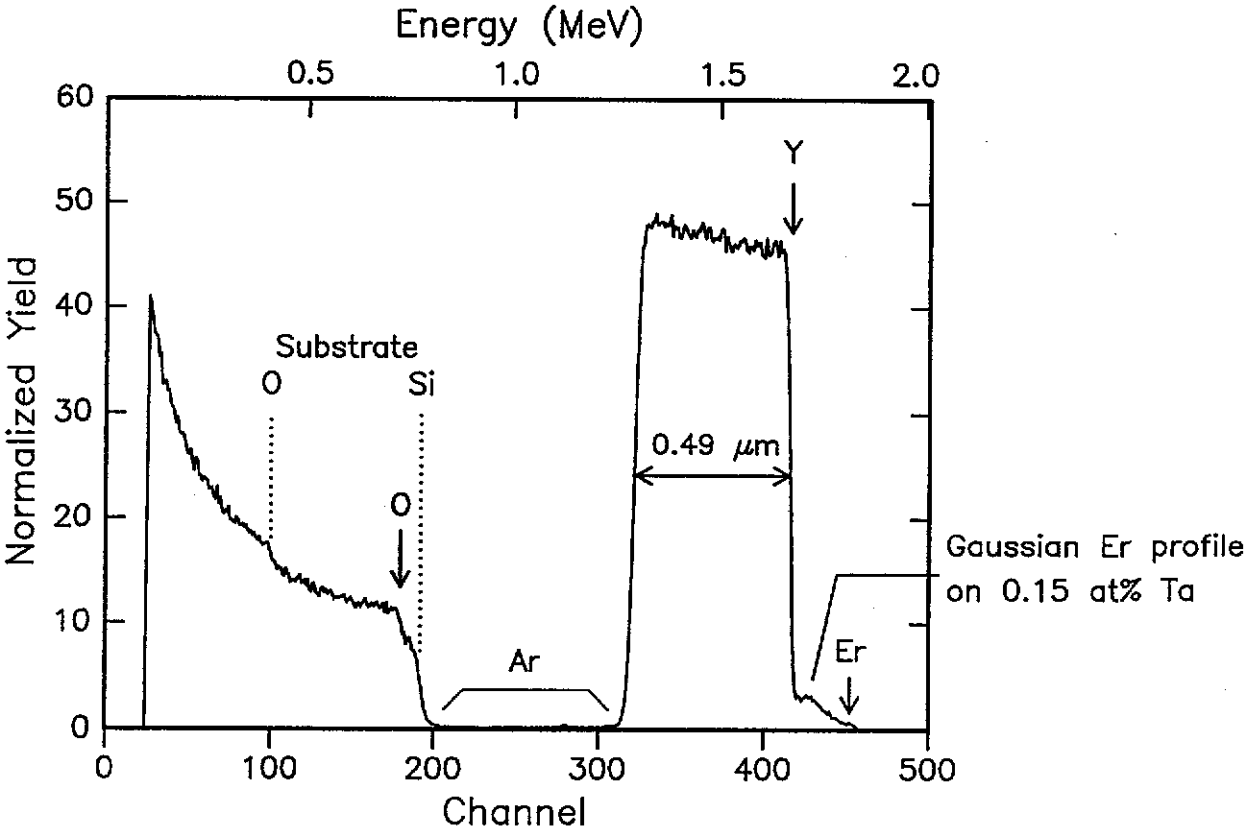

Figure 1: RBS spectrum of an Er-implanted Y_2O_3 film (fluence 1×10^{16} ions/cm^2) on an oxidized Si substrate with 0.15 at% Ta and 0.7 at% Ar contaminations. The O, Y and Er surface channels are indicated. The dotted lines mark the interface channels of the SiO_2 substrate.

2.4 Photoluminescence spectroscopy

Photoluminescence (PL) of the Er-doped films was studied by excitation of the Er ions with a laser beam and spectral analysis of luminescence emitted from the film upon relaxation of the Er ions to the ground state. Luminescence lifetimes were investigated by monitoring the luminescence decay upon excitation with a laser pulse.

An extensive description of the experimental setup which was built for high-intensity in-plane pumping of Er-doped thin films at a wavelength of 1.48 μm can be found in Appendix A. The sample length was 3 mm and the laser was aligned in-plane with the Er-doped layer. Coupling losses were minimized by polishing the sample edges. The laser spot size at the input face was in the order of 2 μm^2 (see section 6.2). The maximum pump power on the sample was 43 mW which corresponds to a laser intensity in the order of 10^6 W/cm^2.

A glass fibre (diameter .8 mm) was positioned normal to the sample surface to collect the luminescence from the high-intensity pumped area of the film. Spectral analysis was performed using a monochromator with a liquid N_2 cooled Ge detector for measurements in the near infrared (wavelength range 0.9 to 1.8 μm) and a photomultiplier tube (PMT) for measurements in the visible part of the spectrum (0.3 to 1.1 μm). The pump laser was mechanically chopped at 14 Hz and the detector signals were lock-in amplified. All PL spectra were corrected for detector sensitivity. Lifetime measurements were performed by monitoring the luminescence decay upon excitation with a laser pulse on a digitising oscilloscope. The oscilloscope pictures were averaged in order to improve the signal to noise ratio. All PL spectroscopy and lifetime measurements were performed at room temperature.

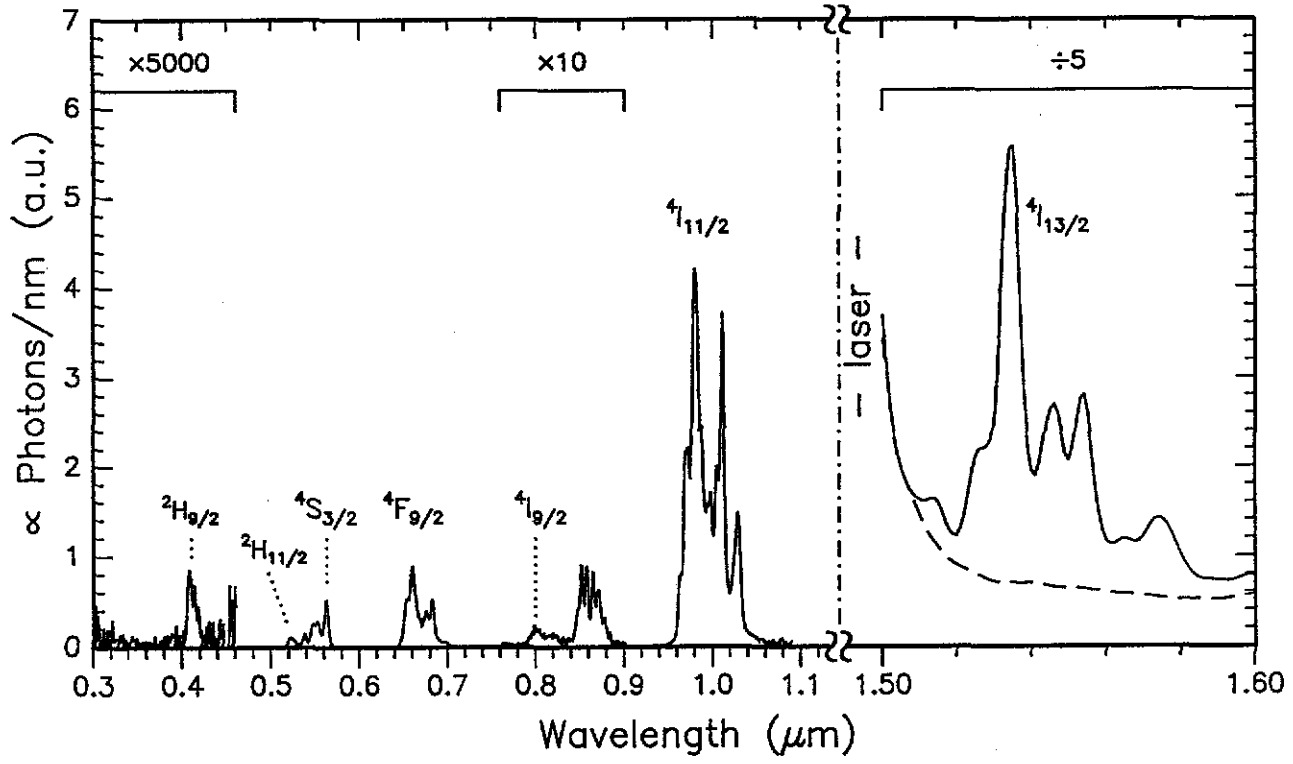

Figure 2: Room temperature PL spectra of an Er-doped Y_2O_3 film (Er fluence 1×10^{16} ions/cm^2, annealed at 700 °C), pumped at 1480 nm, obtained with a PMT (0.3-1.1 μm) and a liquid-N_2 cooled Ge detector (1.1-1.8 μm). The dashed line is due to scattered laser light in the monochromator. The labels refer to excited levels from which transitions to the ground state are observed.

3. Results

3.1 Photoluminescence spectroscopy and lifetime measurements

3.1.1 Experimental results

Figure 2 shows PL spectra of an Er-doped Y_2O_3 film annealed at 700 °C containing an Er dose of 1×10^{16} ions/cm^2 with a peak concentration of 0.75 at%, pumped at 1.48 μm under high intensity conditions (~10^6 W/cm^2 at the focal position). The spectra were acquired using visible and infrared detectors and were corrected for the respective detector sensitivity. The thus obtained PL data is proportional to the number of photons per nanometer. The infrared part of the spectrum (1.5 - 1.6 μm) shows typical Er luminescence peaking at 1534 nm and a background due to scatter of high intensity laser light in the monochromator (measured separately, dashed line). The PMT is insensitive for photons around 1.5 μm and the PL spectrum obtained with this detector does not show any laser-background. The visible part of the spectrum shows clear and manifold peaked luminescence around 980, 660 and 560 nm. Weaker signals were found at 860, 800, 525 and even 410 nm.

Figure 3 shows PL decay measurements as performed at the prominent peak wavelengths of 1534, 980, 660 and 560 nm. The laser pulse shape is indicated. The data is plotted on a logarithmic scale, on which single-exponential data yields a straight line. The 1534 and 660 nm decay curves show clear non-exponential behaviour in the first milliseconds and a single-exponential tail. The 980 nm decay contains a shallow 'bump' and a single-exponential tail and the 560 nm data is single-exponential within the noise level. The tails of the decay data were fitted with a single exponential function of the form

$$PL(t) \propto e^{-\tau/t} \tag{3.1}$$

where t is the time and τ the 1/e lifetime of the decay. The obtained lifetimes are shown in Table 1.

Figure 4 shows normalized 1534 nm PL decay measurements, plotted on a logarithmic scale, at laser pump powers of 4 and 43 mW. The decay rate in the tails is the same for both pump powers, but the fast non-exponential decay during the first few microseconds is more prominent on increasing laser power.

Transition to $^4I_{15/2}$ from	Luminescence wavelength [nm]	1/e Lifetime [ms]
$^4I_{13/2}$	1534	6.0 ± 0.1
$^4I_{11/2}$	980	2.5 ± 0.1
$^4F_{9/2}$	660	0.9 ± 0.1
$^4S_{3/2}$	560	0.9 ± 0.1

Table 1. Initial energy levels of optical transitions to the ground state, peak luminescence wavelengths and 1/e lifetimes

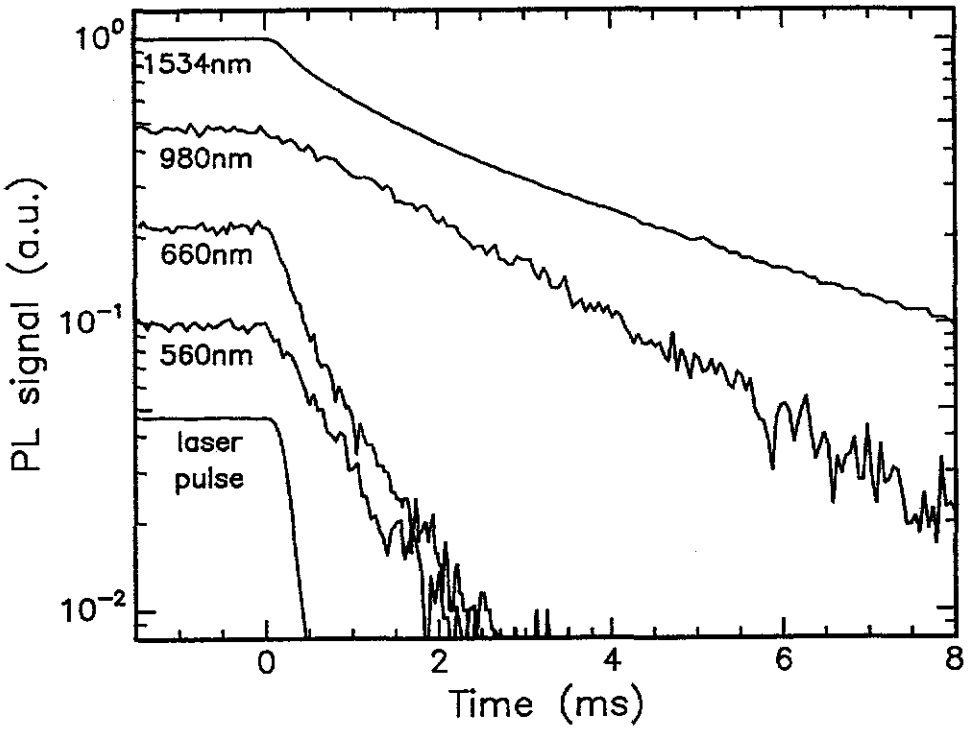

Figure 3: PL intensity decay as a function of time upon pulse excitation, measured at 1534, 980, 660 and 560 nm, plotted on a logarithmic scale. The laser pulse shape is indicated.

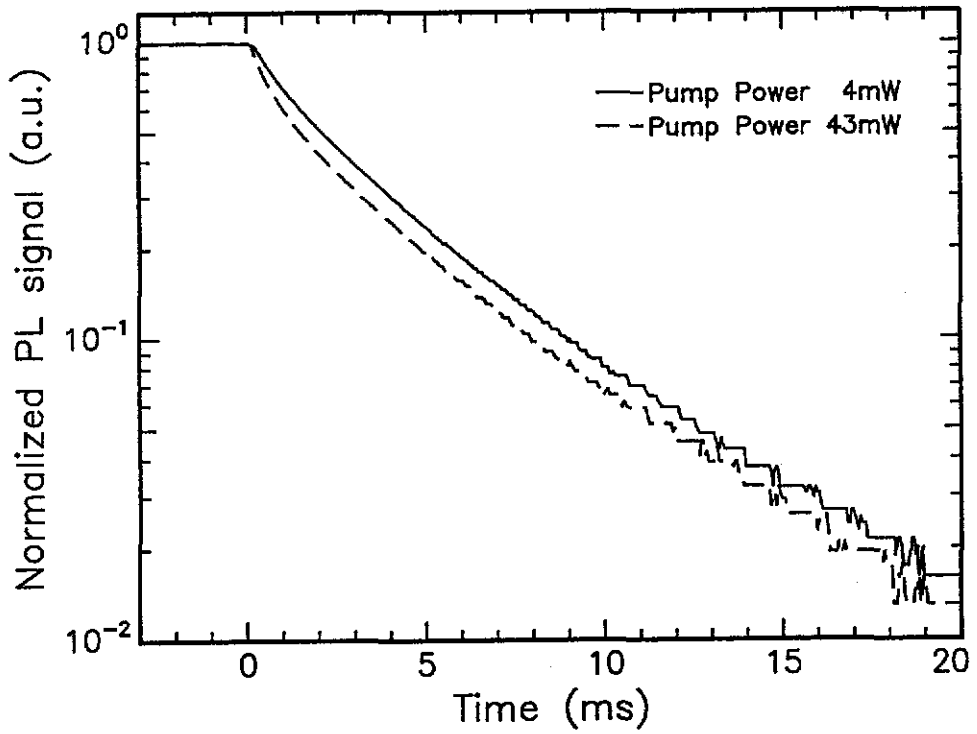

Figure 4: PL intensity decay at 1534 nm, pump power 4 and 43 mW, plotted on a logarithmic scale. The fast, non-exponential decay component shows a clear pump power dependence.

3.1.2 Discussion

Figure 5 shows the energy level scheme (including spectroscopic nomenclature) and the transition wavelengths to the ground state of the Er^{3+} ion in the Y_2O_3 host [6]. The luminescence peaks in Fig. 4 around 410, 525, 550, 660, 800, 980 and 1534 nm can be attributed to radiative decay from respectively the $^2H_{9/2}$, $^2H_{11/2}$, $^4S_{3/2}$, $^4F_{9/2}$, $^4I_{9/2}$, $^4I_{11/2}$ and $^4I_{13/2}$ excited states to the ground ($^4I_{15/2}$) state. The peak around 860 nm can be ascribed to decay from the $^4S_{3/2}$ state to the first excited ($^4I_{13/2}$) state. The broadening of the peaks and the occurrence of a manifold of transition wavelengths is due to Stark splitting of the degenerate energy levels. The sharply resolved peaks show that inhomogeneous broadening of the peaks is small even at room temperature. This is the case when the optically active Er ions are on well defined positions in the crystal. This is most probably an Y site, since the ion radii of Er and Y are approximately equal and the crystal structures of Er_2O_3 and Y_2O_3 are very similar.[1]

The pump power dependence of the fast, non-exponential decay component in the 1534 nm luminescence as shown in Fig. 4 can be explained by ion-ion interactions like cooperative upconversion as will be discussed in section 3.2.4. The slight bump in the 980 nm decay also supports this assumption, as will be explained later.

It must be noted that the lifetimes of the 980, 660 and 560 nm luminescence signals are remarkably long. This indicates that fast non-radiative relaxation of excited Er ions is not prevalent in this material, which is confirmed by the low phonon energy.[7] The strongest fundamental (one-phonon) lattice vibrations in Y_2O_3 occur in the 300-380 cm^{-1} spectral region with a cut-off at 371 cm^{-1}, a very low number compared to the dominant phonon energy in e.g. silica (1100 cm^{-1}). In order to explain the observation in Fig. 2 of the various high-order transitions when pumping (under high intensity conditions) at 1480 nm, first the relation between 1534 nm and 980 nm luminescence is studied as a function of laser pump power.

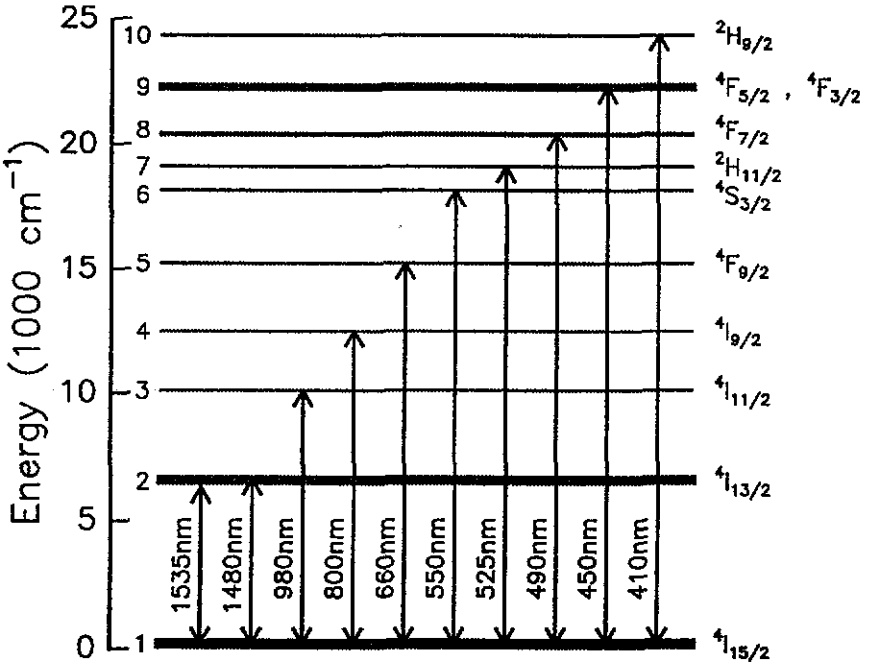

Figure 5: Energy level diagram of the Er^{3+} ion and transition wavelengths for Er in the Y_2O_3 host.

3.2 Pump power dependence of 1534 nm and 980 nm luminescence

The presence of an abundant 980 nm PL signal implies some efficient population mechanism of the $^4I_{11/2}$ level, at the expense of the population of the $^4I_{13/2}$ state. The amplitudes of the PL signals at 1534 nm and 980 nm are proportional to the population densities at the respective energy levels. The relation between the two PL signals in a range of pump powers is studied.

3.2.1 Experimental results

Figure 6 shows the PL signals (proportional to number of photons/nm) at λ = 1534 nm and λ = 980 nm as a function of laser pump power, measured with the Ge detector. Both sets of data are plotted on the same intensity scale. In the low pump power regime up to 15 mW, the slope of the 1534 nm signal shows a steady *de*crease with pump power, whereas the slope of 980 nm signal *in*creases. In the high pump power regime, over 15 mW, the slopes of both signals remain constant.

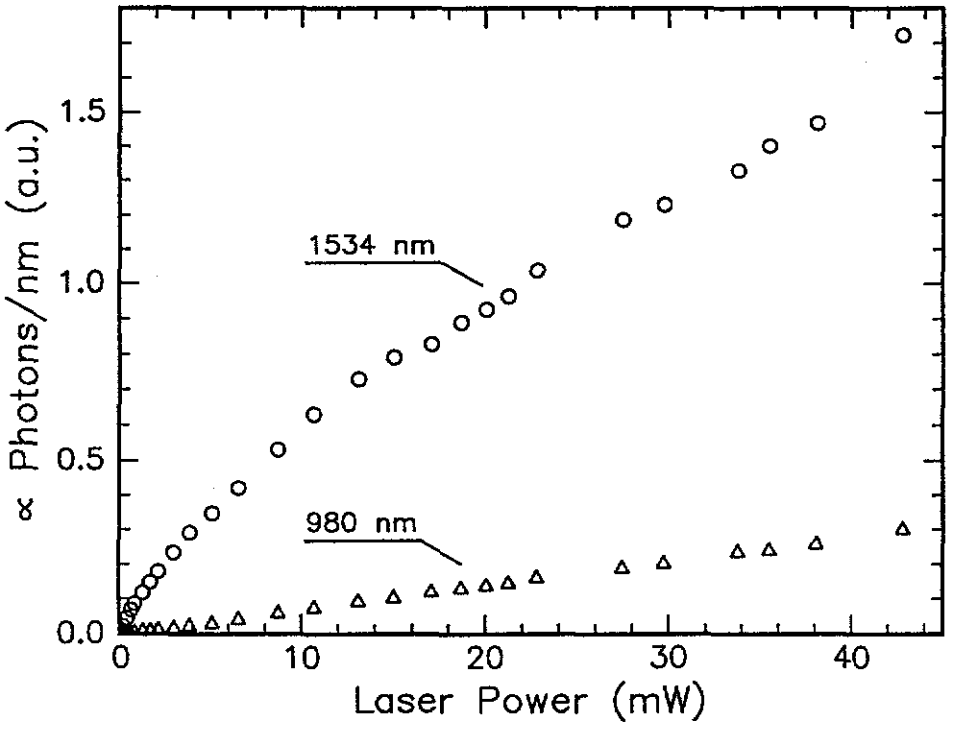

Figure 6: PL peak signals at 1534 nm and 980 nm as a function of pump power.

3.2.2 Discussion

The 1534 nm signal does not show saturation at a certain pump power, despite the high intensity, indicative of the presence of strong depopulation mechanisms. The 980 nm luminescence is observed already at very low pump powers and the identical behaviour of both signals in the high pump power region indicates a correlation between the respective population densities.

The 980 nm luminescence is a result of radiative decay from the $^4I_{11/2}$ level to the ground state. Two models are known for excitation of higher states and subsequent emission of radiation at a shorter wavelength than the pump laser. These mechanisms are Excited State Absorption (ESA) [8] and Cooperative Upconversion (CU) [9,10], both resulting in population of a higher excited state at the expense of the population of the first excited state and therefore degrading the luminescence around 1.53 μm. The two mechanisms show clear differences in their relations between 1534 nm and 980 nm luminescence and will be applied in sections 3.2.3 and 3.2.4 to explain the experimental results.

3.2.3 Excited state absorption

Figure 7a schematically shows the energy diagram of an Er atom and the sequence of the ESA process. An Er atom in the first excited ($^4I_{13/2}$) state absorbs a pump photon (1) and ends up in the $^4I_{9/2}$ state, (2) relaxes non-radiatively to the $^4I_{11/2}$ state and (3a) in most cases relaxes to the first excited state or (3b) might give rise to 980 nm luminescence upon relaxation to the ground state. The rate equations using Einstein notation are

$$\frac{dN_1}{dt} = -R_{12}N_1 - A_{21}N_2 + A_{31}N_3 + S_{21}N_2 \tag{3.1}$$

$$\frac{dN_2}{dt} = R_{12}N_1 - R_{24}N_2 - A_{21}N_2 + A_{32}N_3 - S_{21}N_2 + S_{42}N_4 \tag{3.2}$$

$$\frac{dN_3}{dt} = -(A_{31} + A_{32})N_3 + A_{43}N_4 \tag{3.3}$$

$$\frac{dN_4}{dt} = R_{24}N_2 - A_{43}N_4 - S_{42}N_4 \tag{3.4}$$

where N_x is the population density of level x, x = 1..4 as in Fig. 7a, R_{12} and S_{21} are the pump-absorption and stimulated emission rates, respectively, R_{24} and S_{42} are the excited state absorption (ESA) and stimulated emission rates, respectively and A_{jk} is the spontaneous decay rate from level j to level k. The decay rates A_{42} and A_{41} were neglected because level 4 ($^4I_{9/2}$) decays primarily non-radiatively to level 3. Indeed, Fig. 2 shows only a very low PL signal at 800 nm.

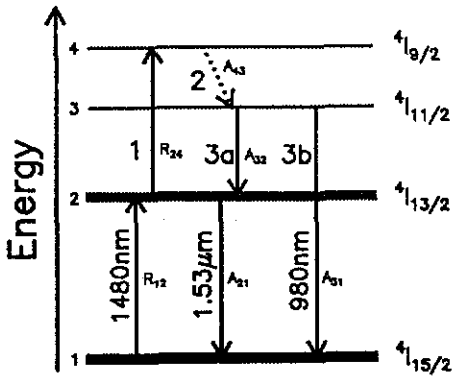

Figure 7a: Schematic of the ESA mechanism in the energy level diagram of the Er^{3+} ion.

Under steady state conditions all time derivatives are equal to zero and using (3.3) and (3.4) while neglecting S_{42} ($<<A_{43}$), this leads to a relation between the population densities N_3 and N_2:

$$N_3 = \frac{R_{24}}{A_{31}+A_{32}} N_2 = R_{24}\,\tau_3\,N_2 \qquad (3.5)$$

where τ_3 is the 1/e lifetime of level 3, i.e. the 980 nm PL lifetime as stated in Table 1. The PL intensity I is proportional to the population density N via the decay rate A:

$$I_{980\,nm}(P) \propto N_3(P)\times A_3(P) = \frac{N_3(P)}{\tau_3} \qquad (3.6)$$

where I_{980} is the PL intensity at 980 nm and P the pump power, assuming $A_3(P) = (\tau_3)^{-1}$. An equivalent relation can be found for $I_{1534}(P)$, the PL intensity at 1534 nm as a function of pump power. Lifetime measurements discussed in section 3.2.1 show a clear pump power dependence and non-exponential behaviour in the decay curves, presumably due to Er-Er interactions. However, a single-exponential component independent of pump power has been obtained from the tails of the curves, which may be used here. Combining (3.5) and (3.6) leads to the following relation between the PL intensities at 1534 and 980 nm for the ESA mechanism:

$$\frac{I_{980}(P)}{I_{1534}(P)} \propto \frac{N_3(P)}{N_2(P)} \propto R_{24} \propto P \qquad (3.7)$$

Figure 7b shows the I_{980}/I_{1534} curve as a function of pump power. It is clear that the dependence on pump power is not linear as expected from (3.7), which means that this ESA model does not give a complete description of the excitation mechanism of the $^4I_{11/2}$ level.

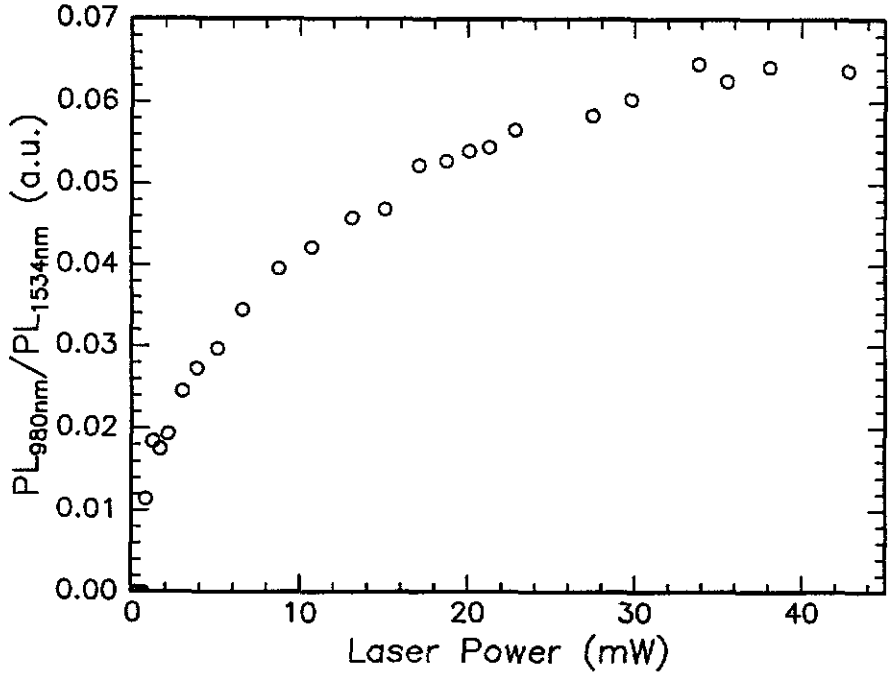

Figure 7b: Ratio of PL peak signals at 980 nm and 1534 nm as a function of pump power. The ESA model predicts a linear dependence on pump power.

3.2.4 Cooperative upconversion

If cooperative upconversion (also called: cross-relaxation induced upconversion) takes place, two atoms are involved (they cooperate) in the excitation to the $^4I_{11/2}$ state. Figure 8a depicts the upconversion sequence: (1) Two neighbouring atoms are excited to the first excited ($^4I_{13/2}$) state by two 1.48 μm pump photons. (2) Energy is transferred from one atom (donor) to the other atom (acceptor). The energy-transfer results in a de-excited donor atom and an acceptor atom in the $^4I_{9/2}$ state, which will decay analogous to the ESA case described in section 3.2.3. Emission of 800 nm luminescence is neglected. Rapid decay to the $^4I_{11/2}$ state (3) is followed by relaxation to the ground state (4) via the first excited ($^4I_{13/2}$) state or directly under emission of a 980 nm photon.

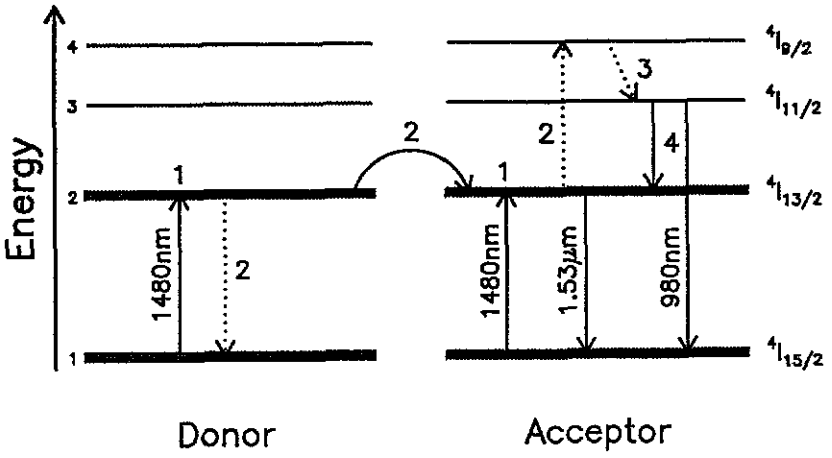

Figure 8a: Schematic of the cooperative upconversion mechanism from the $^4I_{13/2}$ state.

The rate equations for this two-particle model are:

$$\frac{dN_1}{dt} = -R_{12}N_1 + A_{21}N_2 + C_2\left(N_2\right)^2 + A_{31}N_3 \tag{3.8}$$

$$\frac{dN_2}{dt} = R_{12}N_1 - A_{21}N_2 - 2C_2\left(N_2\right)^2 + A_{32}N_3 \tag{3.9}$$

$$\frac{dN_3}{dt} = -(A_{31} + A_{32})N_3 + A_{43}N_4 \tag{3.10}$$

$$\frac{dN_4}{dt} = C_2\left(N_2\right)^2 - A_{43}N_4 \tag{3.11}$$

where N_x is the population density of level x, R_{12} the pump-absorption rate of level 2, A_{jk} the spontaneous decay rate from level j to level k and C_2 the upconversion coefficient. Two particles are involved, introducing quadratic terms in the rate equations. Similar to the ESA model in the previous section the decay rates A_{42} and A_{41} are neglected with respect to the fast non-radiative A_{43}.

Under steady state conditions the time derivatives are equal to zero and combining (3.10) and (3.11) leads to a quadratic relation between the population densities N_3 and N_2:

$$N_3 = \frac{C_2}{A_{31}+A_{32}}(N_2)^2 = C_2\,\tau_3\,(N_2)^2 \qquad (3.12)$$

which implies a similar correlation between the PL intensities at 1534 nm and 980 nm:

$$I_{980} \propto (I_{1534})^2 \qquad (3.13)$$

Figure 8b shows the PL intensities at 980 nm versus 1534 nm on log/log scale. The slope is 1.58, which is not in agreement with (3.13) from which a slope of 2 is expected. From this can be concluded that the upconversion model as depicted in Fig. 8a does not give a correct description of the excitation mechanism leading to 980 nm luminescence.

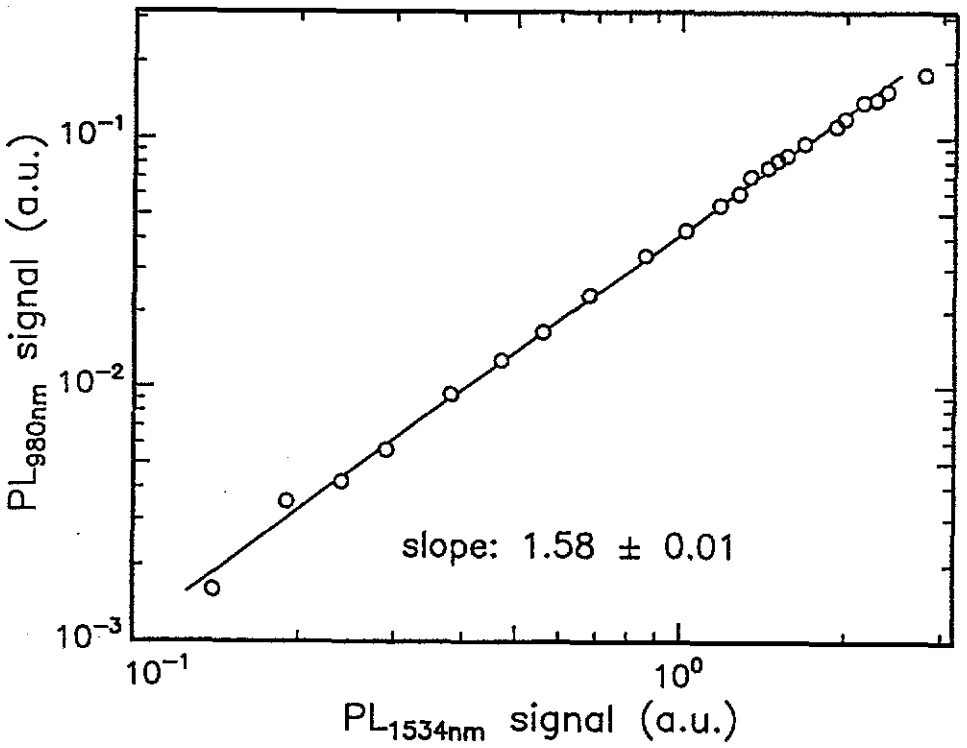

Figure 8b: PL peak signal at 980 nm versus 1534 nm on a log/log scale. The cooperative upconversion model predicts a slope of 2.

3.3 Higher order effects

In both models as mentioned above, the population densities of higher excited states were considered negligibly small compared to the populations of the $^4I_{15/2}$, $^4I_{13/2}$ and $^4I_{11/2}$ levels and were accordingly left out of the rate equations. However, when taking into account the relatively long lifetime of the $^4I_{11/2}$ state (τ = 2.5 ms) a considerable population density of this level can be expected even at modest pump powers, enhancing the probability of subsequent excitation to higher states. This means that higher order effects might play a more important role than expected. In the next sections, population of higher states at the expense of the $^4I_{11/2}$ state is taken into account. The population density of the $^4I_{9/2}$ state is negligible, as was concluded from the minute luminescence signal in Fig. 2 around 800 nm, hence no excitations from this level are taken into account for populating higher states.

3.3.1 Green luminescence at 560 nm

Figure 2 shows a luminescence peak at 560 nm, attributed to the transition from the $^4S_{3/2}$ level to the ground state. Figure 9 shows the PL intensities at 980 nm and 560 nm vs. pump power, measured with the PMT. Both sets of data are plotted on the same intensity scale. Two mechanisms can be responsible for the population of $^4S_{3/2}$ from the $^4I_{11/2}$ level; ESA or CU. The energy difference between the $^4I_{11/2}$ and the $^4S_{3/2}$ levels[11] is 8040 cm^{-1}, whereas a 1480 nm pump photon, the driving force in the ESA model, has an energy of only 6760 cm^{-1}. This means that ESA from the $^4I_{11/2}$ level can be rejected as a possible explanation of the 560 nm luminescence.

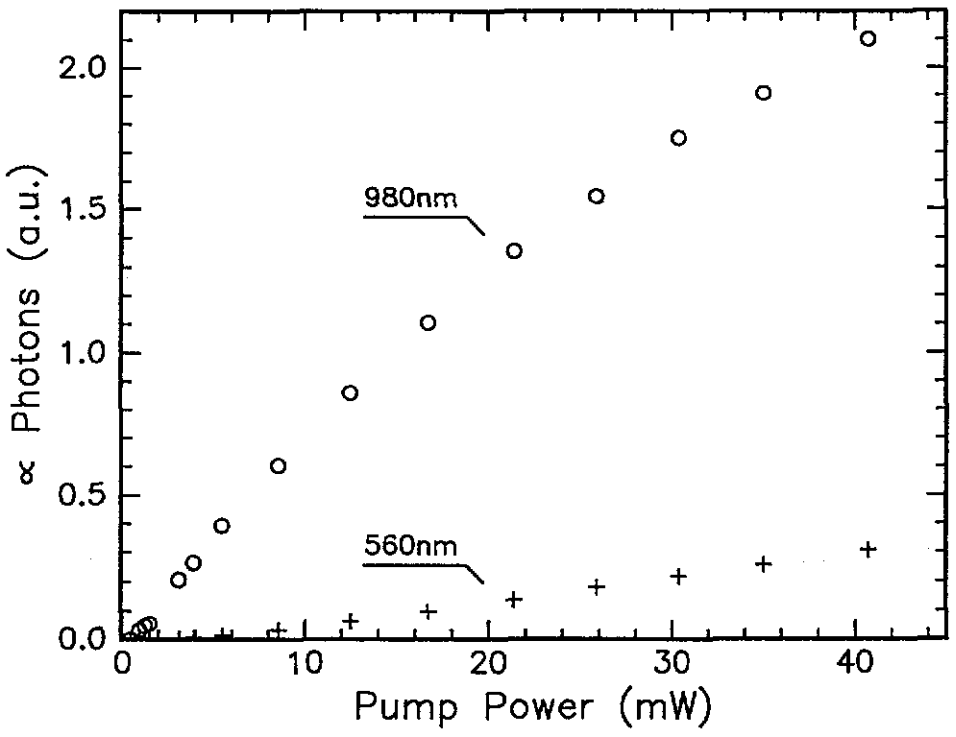

Figure 9: PL peak signals at 980 nm and 560 nm as a function of pump power.

A more feasible mechanism is cooperative upconversion as depicted in Fig. 10a, a scaled-up analogy to the model in Fig. 8a. (1) Two neighbouring atoms are both excited to the $^4I_{11/2}$ state. (2) Energy is transferred from the donor to the acceptor atom, resulting in a de-excited donor atom and an acceptor atom in the $^4F_{7/2}$ state. (3) The acceptor atom relaxes rapidly to the $^4S_{3/2}$ level and gives rise to luminescence around 560 nm.

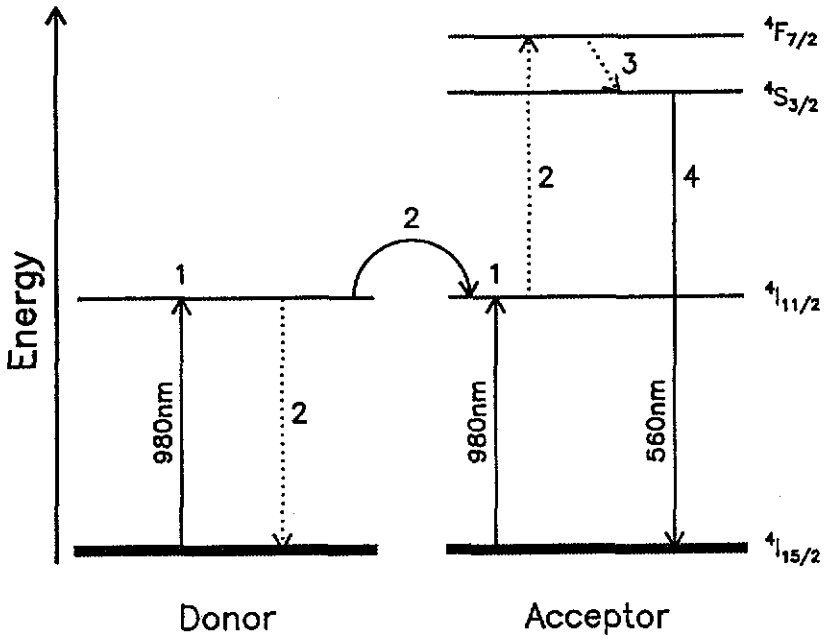

Figure 10a: Schematic of the cooperative upconversion mechanism from the $^4I_{11/2}$ state in the Er^{3+} ion.

The relevant rate equations for the $^4F_{7/2}$ and $^4S_{3/2}$ levels are:

$$\frac{dN_8}{dt} = -A_{86}N_8 + C_3(N_3)^2 \tag{3.14}$$

$$\frac{dN_6}{dt} = A_{86}N_8 - A_6N_6 \tag{3.15}$$

In steady state a quadratic relation is found between the 560 nm and 980 nm PL intensity:

$$A_6N_6 = C_3(N_3)^2 \Rightarrow N_6 \propto (N_3)^2 \Rightarrow I_{560} \propto (I_{980})^2 \tag{3.16}$$

Figure 10b shows the PL signal at 560 nm versus 980 nm on log/log scale taken at different pump powers. The slope of 1.98 ± 0.10 is in excellent agreement with the two-particle model and proves that in this sample the 560 nm light is a result of cooperative upconversion from the $^4I_{11/2}$ state.

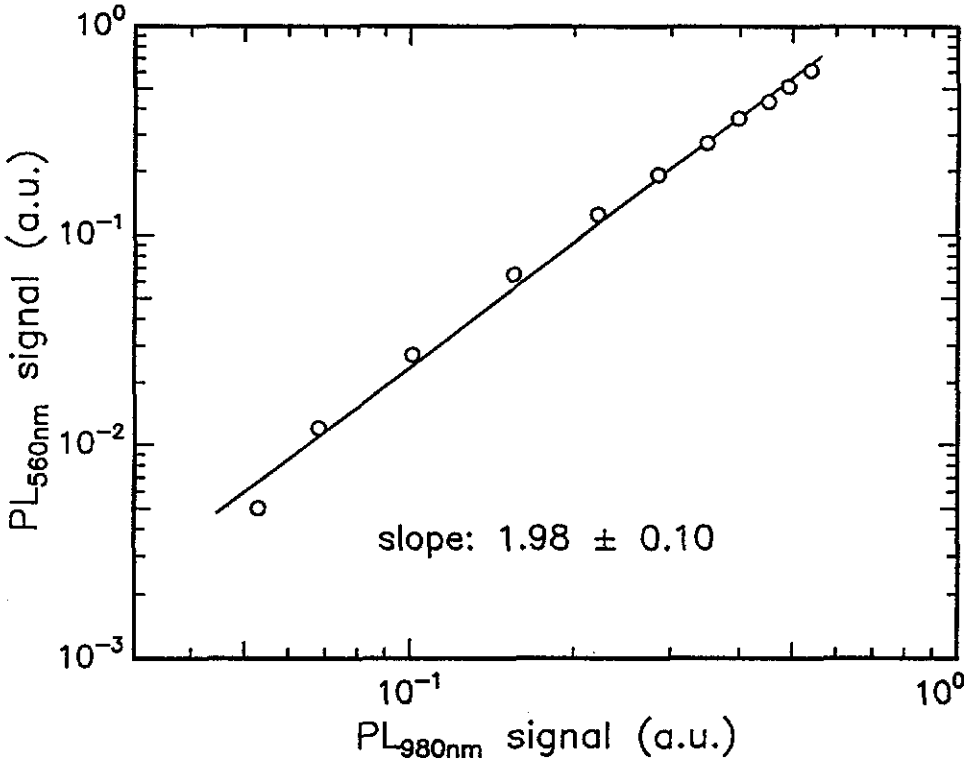

Figure 10b: PL peak signals at 560 nm vs. 980 nm on a log/log scale. The slope of 2 is in agreement with the modelled two-particle mechanism for cooperative upconversion.

3.3.2 Other higher order effects

Apart from the 560 nm light, the spectrum in Fig. 4 shows luminescence at several other wavelengths smaller than the pump wavelength. A prominent contribution is found at 660 nm which can be attributed to the same excitation which is responsible for the 560 nm and 525 nm luminescence; population of the $^4F_{7/2}$ state by means of upconverted 980 nm light and non-radiative decay to the $^4F_{9/2}$ state followed by 660 nm luminescence to the ground state. The very small ultra-violet contribution at 410 nm can be attributed to the transition from $^2H_{9/2}$ to the ground state and might be a result of ESA of an Er ion in the $^4S_{3/2}$ state. The energy difference between the two levels is 6210 cm^{-1} which can be matched reasonably well with a 1480 nm pump photon (6760 cm^{-1}). The 410 nm luminescence may also originate from upconversion involving Er ions in the $^4S_{3/2}$ and $^4I_{13/2}$ state. No pump power dependence of these higher order effects has been studied. Once again it is noted that the lifetime of both 660 and 560 nm signals are as long as 0.9 ms.

3.3.3 Corrections on the models of ESA and cooperative upconversion

In the sections 3.2.3 and 3.2.4 neither the proposed ESA model nor the CU model could explain the relation between the obtained 1534 nm and 980 nm PL data. A complete correction of the models for all observed 'parasitic' depletion of the $^4I_{11/2}$ level to higher excited states is not conceivable. However, the presence of 560 nm luminescence has been identified in section 3.3.1 as a pure cooperative upconversion effect which can be added in that form to the rate equations concerning the $^4I_{11/2}$ level. In steady state the following relations of N_2 and N_3 can be found:

- in the case of excited state absorption:

$$R_{24}N_2 = \frac{N_3}{\tau_3} + C_3 (N_3)^2 \quad , \quad R_{24} \propto \text{Pump} \tag{3.17}$$

- in the case of cooperative upconversion:

$$C_2(N_2)^2 = \frac{N_3}{\tau_3} + C_3 (N_3)^2 \tag{3.18}$$

in which R_{24} is the pump rate of the $^4I_{9/2}$ level due to excited state absorption of pump photons by the $^4I_{13/2}$ level, C_2 the upconversion coefficient for the population of the $^4I_{9/2}$ level and C_3 the 'green' upconversion coefficient for population of the $^4F_{7/2}$ level. In order to find out whether one of these enhanced models can explain the PL data, the population densities N_2 and N_3 in (3.17) and (3.18) were replaced by the respective PL signals I_{1534} and I_{980} via:

$$N_2 = \frac{I_{1534}}{A_{21}\varepsilon} = \frac{I_{1534}\tau_2}{\varepsilon} \tag{3.19}$$

$$N_3 = \frac{I_{980}\tau_3}{\varepsilon} \tag{3.20}$$

in which ε is proportional to the collection efficiency.

Also the ESA pump rate R_{24} was rewritten:

$$R_{24} = \frac{\sigma_{24}}{h\nu} I_{laser} = \frac{\sigma_{24}}{h\nu}\frac{P}{A} \tag{3.21}$$

in which σ_{24} is an excited state absorption cross section, $h\nu$ is the pump photon energy, I_{laser} the laser pump intensity, P the pump power and A the area of the laser spot on the sample. Incorporating (3.19), (3.20) and (3.21) into (3.17), we obtain a new expression for the ESA model:

$$P(I_{1534}) = \frac{h\nu A}{\sigma_{24}\tau_2}(I_{980}) + \frac{C_3 h\nu A (\tau_3)^2}{\varepsilon \sigma_{24}\tau_2}(I_{980})^2 \tag{3.22}$$

Figure 11 shows the 1534 nm PL signal multiplied by the pump power on the vertical axis and the 980 nm PL signal on the horizontal axis. In order to test (3.22), a fit of the form

$$f(x) \;=\; a\,x^2 + b\,x \tag{3.23}$$

was applied and the fit parameters were found to be

$$a = \frac{C_3\,h\nu\,A}{\varepsilon\,\sigma_{24}}\frac{\tau_3^{\,2}}{\tau_2} = 0.677\ \mathrm{J\,s^{-1}} \quad , \quad b = \frac{h\nu\,A}{\sigma_{24}\,\tau_2} = 4.42\times10^{-2}\ \mathrm{J\,s^{-1}} \tag{3.24}$$

From parameter b the absorption cross section σ_{24} can be calculated. The other constants are known; laser spot size $A \approx 3\times10^{-7}$ cm^2, $h\nu = 1.34\times10^{-19}$ J, $\tau_2 = 6.0$ ms. This yields an absorption cross section $\sigma_{24} \approx 1.5\times10^{-22}$ cm^2. This value is one order of magnitude smaller than the pump absorption cross section of the first excited state σ_{12} which is typically 1.5×10^{-21} cm^2 for Er-doped planar Y_2O_3 films.[6] This analysis suggests that the data in Fig. 11 can be fitted with the ESA model of (3.22).

With equivalent methods we can check the validity of the CU model in (3.18) by substitution of the population densities with the respective PL signals:

$$\left(I_{1534}\right)^2 \;=\; \frac{\varepsilon}{C_2\left(\tau_2\right)^2}\left(I_{980}\right) + \frac{C_3}{C_2}\left(\frac{\tau_3}{\tau_2}\right)^2\left(I_{980}\right)^2 \tag{3.25}$$

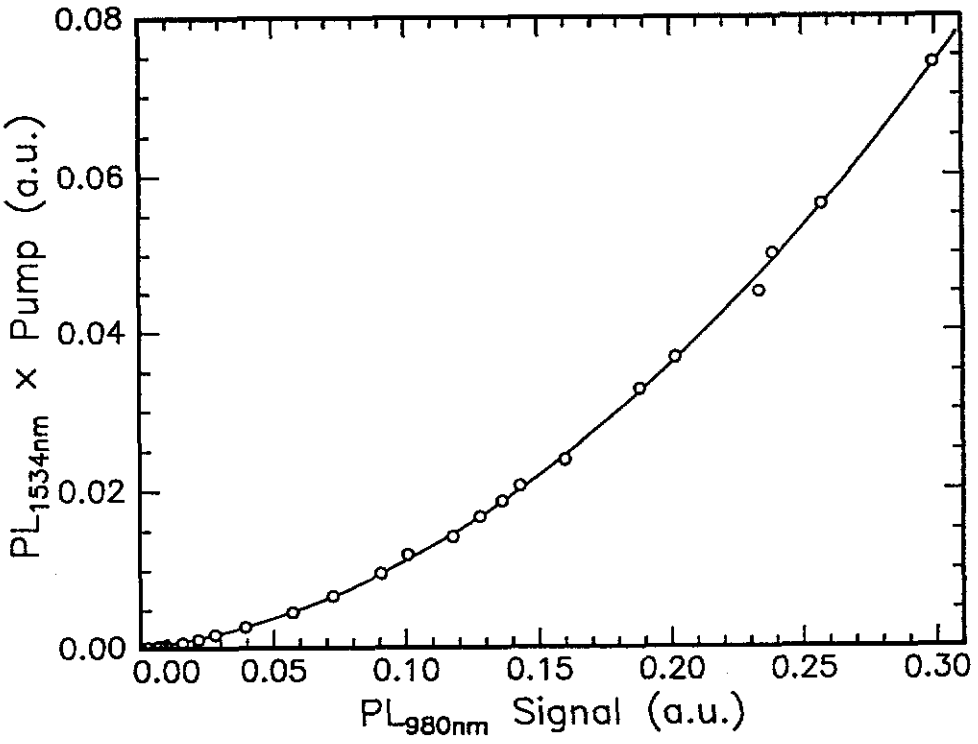

Figure 11: PL at 1543 nm × Pump power vs. PL at 980 nm. The solid line is an ESA fit corrected for upconverted 560 nm luminescence.

Figure 12 shows the PL signal at 1534 nm vs. 980 nm at various pump powers. A fit of the form

$$f(x) = \sqrt{a\,x^2 + b\,x} \tag{3.26}$$

was applied and the fit parameters were found to be

$$a = \frac{C_3}{C_2}\left(\frac{\tau_3}{\tau_2}\right)^2 = 19 \quad , \quad b = \frac{\varepsilon}{C_2\,(\tau_2)^2} = 3.7 \tag{3.27}$$

From parameter a the ratio of the upconversion coefficients can be calculated. The single-exponential components of the lifetimes τ_2 and τ_3 are 6.0 ms and 2.5 ms respectively, which yields $C_3 = 109\ C_2$. Hence the CU model predicts that the 980 nm upconversion process, generating the 560 nm luminescence, has an energy transfer resulting in cooperative upconversion two orders of magnitude more efficient than the coupling between two ions in the first excited state, producing 980 nm luminescence.

The upconversion coefficients can be calculated roughly by estimating the degree of inversion of the first excited state in this sample. When assuming a population of the $^4I_{13/2}$ level of roughly 30% and P = 43 mW, $I_{1534} = 1.5$ (see Fig. 12), Er concentration 0.75 at%, atomic density of Y_2O_3 0.67×10^{23} at/cm^3, from (3.19) the efficiency term ε can be derived: 6×10^{-23} cm^{3}s. Using (3.27) the upconversion coefficients C_2 and C_3 are found: respectively 5×10^{-25} m^{3}s^{-1} and 5×10^{-23} m^{3}s^{-1}. It is also possible to calculate the 560 nm upconversion coefficient C_3 from the ESA model fit parameter a in (3.24a). This yields a value for C_3 of 1×10^{-22} m^{3}s^{-1} which is in the same order of magnitude as the results of the CU model.

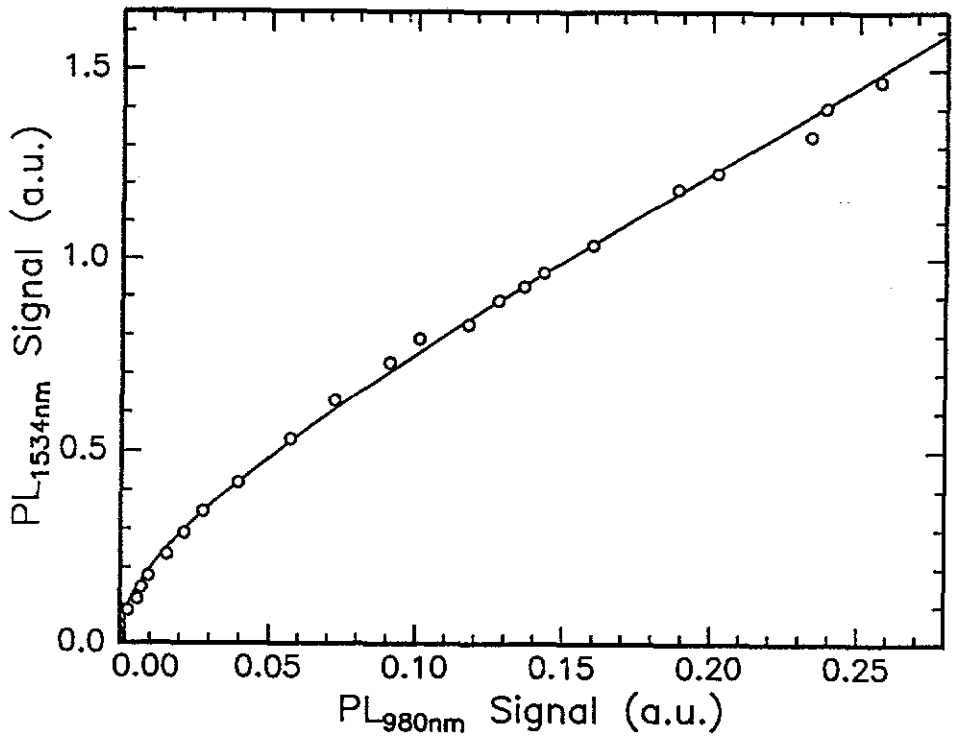

Figure 12: PL at 1543 nm vs. PL at 980 nm. The solid line is a cooperative upconversion fit corrected for upconverted 560 nm luminescence.

Both models produce reasonable numbers, but contain some assumptions, making the calculations too crude to trust the results completely. However, one important feature in the luminescence data is not yet taken into account. Figure 4 shows decay measurements with a clear non-exponential behaviour which becomes more prominent upon increasing pump power. This fast drop of the luminescence intensity in the first few milliseconds cannot be explained by excited state absorption. Figure 7a shows the ESA sequence. Switching off the laser causes the population in the $^4I_{13/2}$ level to decay spontaneously to the ground state with single-exponential behaviour. However, any decay from higher excited states will replenish the $^4I_{13/2}$ level and *slow down* the decay non-exponentially during the first few milliseconds. However, the data in Fig. 4 shows the opposite behaviour – a fast decrease of the luminescence intensity – which can only be explained by the cooperative upconversion process as shown in Fig. 8a. Even after switching off the laser, fast depletion to the ground state occurs when two ions in the first excited state interact, generating extra 980 nm luminescence, explaining the slight bump in the 980 nm decay data in Fig. 3. It can be concluded that in this case of high-intensity 1480 nm pumping of Er-implanted Y_2O_3 thin films, cooperative upconversion involving ions in the $^4I_{13/2}$ state is the main cause of the population of the $^4I_{11/2}$ level.

4. Conclusions

In this work, photoluminescence properties of Er-implanted Y_2O_3 planar optical waveguides pumped at a wavelength of 1.48 μm under high intensity conditions (~10^6 W/cm^2) were studied. The samples were implanted with 1×10^{16} Er/cm^2 at 800 keV to a Er peak concentration of 0.75 at%, and subsequently annealed at 700°C for 1 hour. Photoluminescence measurements at room temperature using infrared and visible detectors show sharply peaked Er luminescence not only at a wavelength of 1.53 μm but also in the spectral region between 0.41 and 1 μm, indicating a considerable population in various higher states than the pump band. Relatively long luminescence lifetimes of 6.0, 2.5, 0.9 and 0.9 ms were found for respectively the $^4I_{13/2}$, $^4I_{11/2}$, $^4F_{9/2}$ and $^4S_{3/2}$ states indicating that fast non-radiative decay from these levels is not prevalent. This is a result of the low phonon energy in the heavy-metal oxide host. The decay curves from the $^4I_{13/2}$ and $^4F_{9/2}$ levels also contain a clear non-exponential component which can be attributed to ion-ion interactions leading to cooperative upconversion. This effect shows a pump power dependence.

A strong 980 nm signal is observed. PL decay data strongly indicates cooperative upconversion from the first ($^4I_{13/2}$) excited state to be its driving force. Subsequent cooperative upconversion from the $^4I_{11/2}$ state is observed resulting in luminescence at 560 nm from the $^4S_{3/2}$ state. A small signal in the near-UV is attributed to excited state absorption of the $^4S_{3/2}$ state; a third order effect.

The observed depopulation mechanisms of the 1.54 μm lasing level in this material will severely limit its application in active planar optical devices like planar optical amplifiers in which a high degree of inversion of the first excited state is of vital importance. This work shows that cooperative upconversion is the most important depopulation process, putting an upper limit to the peak Er concentration, as cooperative upconversion is strongly concentration dependent. However, the observed efficient production of green luminescence and long lifetimes of several higher energy levels makes high-concentration Er-implanted Y_2O_3 films a promising candidate for producing planar IR-pumped green upconversion lasers at 560 or 660 nm.

5. Acknowledgments

Numerous people have assisted me during my Eigen Werk III and IV practical training periods at AMOLF. I would like to mention the following persons in particular.

Dr. T. Hoekstra and Dr. P.V. Lambeck (Univ. Twente) are gratefully acknowledged for providing sputter-deposited Y_2O_3 films. Dr. B. Verbeek (Philips) is acknowledged for providing high-power laser diodes. Ir. C. van Dam and Ir. M. Amersfoort (TU Delft) have produced many practical answers to my questions during the months of designing the laser to fiber coupling and the waveguide coupling setup.

Op het AMOLF ben ik R. Koper veel dank verschuldigd voor hoogwaardig polijstwerk. Ook J. Derks, J. ter Beek, P. Kea en W. Brouwer wil ik bedanken voor de technische ondersteuning.

The members of the sections Ion Implantation and New Materials at AMOLF are acknowledged for the fruitful discussions and support. Special acknowledgments go to Drs. G.N. van den Hoven and Drs. E. Snoeks, who committed a lot of time to my setup and experiment and who put me 'back on the track' when I pondered over details. Dr. A. Polman provided me with the exceptional opportunity of building a high-tech experimental setup and he showed me what a tremendous amount of physics can be extracted from just one experiment. The students in 'Er^{3+} een schepje bovenop' room H048, Pieter and Mark, provided cheerful hours in- and outside the lab.

6. Appendix A

6.1 Experimental setup for coupling of laser to fiber (Fig. 13)

The key component of the experiment is the solid-state laser, a high-power InGaAsP laser diode lasing in the near-infrared at $\lambda = 1.48$ µm, which produces over 100 mW of optical power at a current of 750 mA max. The diode is fitted in a TO5 transistor can and is placed in a laser diode mount with a thermoelectric (Peltier) cooled heatsink. A diode laser controller supplies a stabilised diode current and regulates the temperature of the heatsink. Flexible and non-hazardous manipulation of the pump light while maintaining a good beam quality is ensured when using an optical fiber for guiding the laser light into the experiment. A coupling setup for this purpose is built on a separate breadboard and is schematically depicted in Fig. 13.

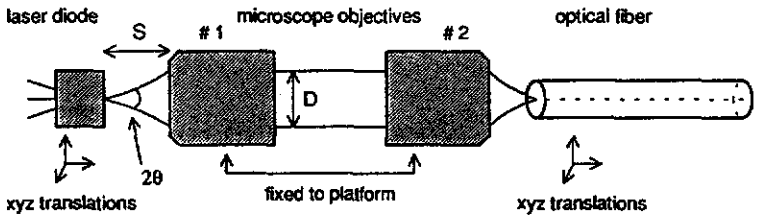

Figure 13: Schematic of optical coupling of laser diode output into optical fiber using two microscope objectives.

Coupling of the laser output into a fiber is done with two microscope objectives, one objective (#1) collects and collimates the laser output, the second (#2) focuses the collimated beam onto the fiber tip and into the fiber core. Microscope objectives are used for this task because of the high quality of their optical components and their design for collimation of near-infrared sources and precise focusing of laser beams. The choice of magnification ratios of the microscope objectives depends on the optical specifications of the laser diode and the fiber.

Laser diodes produce a diverging elliptical radiation pattern with a typical diverging angle between 20° and 45°, the diode in this work has a nominal emission angle of 40°. The ellipticity stems from different diffractive indices at the laser cavity boundaries. The emission can be described as a Gaussian beam since both the electric field and the power density obey a Gaussian error function. The laser output is linearly polarized; the orientation of the electric field is parallel to the laser junction.

The fiber is a standard Siecor pure silica fiber with a nominal core diameter of 8.3 µm and a cladding of 125 µm. The fiber ends are terminated with so-called FC/PC connectors. The fiber core has a slightly

higher refractive index ($\Delta n = 0.36\%$) than the cladding, causing total internal reflection of light at the core-cladding interface when light propagates through the fiber. Due to the small core diameter this fiber is *singlemode* for wavelengths over 1.2 μm, which means that only one mode can propagate through the fiber for those wavelengths. This fundamental mode propagates in a straight fashion without reflections at the boundary between core and cladding. The ray optics model (total internal reflection at the core/cladding boundary) fails to describe the propagation of light through a singlemode fiber. Instead, wave optics have to be applied.[12] The electromagnetic field of the fundamental mode forms a Gaussian error function. The mode-field diameter is larger than the physical core diameter and is wavelength-dependent. The Siecor fibers have a nominal mode diameter w of 9.3±0.5 μm (FWHM) at 1300 nm and 10.5±1.0 μm at 1550 nm. When light travels through the fiber in this Gaussian mode, the fiber shows a very low loss; typically 0.2 dB/km at a wavelength of 1550 nm. It should be noted that in this standard fiber the direction of polarization is not preserved; that should be done utilising a polarization-maintaining fiber. In this work however no special interest is paid to the polarized nature of the laser light.

The key parameter for describing either the acceptance angle of a lens or the emission angle of a light source is the Numerical Aperture NA:[13]

$$NA = n_0 \sin\theta \tag{6.1}$$

where 2θ is the full acceptance (or emission) angle and n_0 is the refractive index of the medium, in this case the air. The nominal laser diode emission angle θ is 40° which corresponds to a NA of 0.64.

For (singlemode) fibers the NA can be calculated from the refractive indices in the fiber:[13]

$$NA = \sqrt{n_1^2 - n_2^2} \tag{6.2}$$

where n_1 is the core refractive index, n_2 the cladding refractive index. The Siecor singlemode fiber has a nominal NA of 0.13.

Two requirements should be met for optimal coupling of the laser to the fiber:

1. The numerical apertures of the collecting and focusing microscope objectives are matched to the respective numerical apertures of laser diode (NA 0.64) and singlemode fiber (NA 0.13).
2. The incident field distribution is matched to that of the fiber field mode. That is done by focusing the Gaussian beam down to a spot of comparable size as the field diameter of 10 μm.

NA-matching is performed using commercially available standard microscope objectives featuring NA = 0.65 and 0.12 with working distances S of 0.4 and 6 mm respectively. The objectives are commonly identified by their magnification ratios, being 40x and 4x respectively.

The laser light is collimated by placing the laser diode in the focal point of microscope objective #1, i.e. at the working distance.

The collimated beam diameter D can be calculated using the focal length F and the NA of the microscope objective:[13]

$$\tan\theta = \frac{D}{2F} \quad \Rightarrow \quad D = 2F\tan\left(\arcsin\frac{NA}{n_0}\right) \tag{6.3}$$

and for the 40x microscope objective this yields a beam diameter D of 7.5 mm. The collimated beam is focused onto the fiber tip using microscope objective #2. The focal spot diameter w_0 for Gaussian beams depends on the diameter of the collimated beam entering the lens and its focal length:[13]

$$w_0 = \frac{4\lambda}{\pi}\frac{F}{D} \tag{6.4}$$

where λ is the wavelength of the light and w_0 is defined at $1/e^2$ of maximum power density. Neglecting the elliptical beam shape of the laser output and using (5.4), the diffraction limited spot diameter w_0 of the light focused by the 4x objective is found to be 7.9 μm. In practice the elliptical beam shape is not negligible. Measurements done by scanning the fiber tip through the focal area and measuring the laser power after the fiber show that a spot diameter of 10 to 12 μm can be obtained in this setup and that the spot also has a slight elliptical shape.

The 40x microscope objective has a broadband anti-reflection coating for the wavelength range of 1300 to 1550 nm. The 4x lens is uncoated. The 4x and 40x microscope objectives are placed at 180° with respect to each other into an RMS-threaded mount and are rigidly attached to the breadboard. Precise and stable alignment of the fiber and the laser diode with respect to the microscope objectives is performed with micropositioning stages (so-called Microblocks) for XYZ-translations with a resolution of 0.5 μm in the three directions.

An unexpected phenomenon occurs when operating the laser diode at high powers (I > 300 mA). After switching on it takes a period of more than half an hour for the alignment of laser to fiber to stabilize in a reproducible way. This might be caused by thermal expansion and misalignment inside the laser diode itself or the closely positioned 40x microscope objective. Repetitive 'warming up' and 'cooling down' did not significantly affect the alignment or incoupling efficiency. A checklist of a complete alignment procedure of laser to fiber can be found in Appendix B.

6.2 In-plane coupling of laser to thin films (Fig. 14)

In this setup we couple the 1.48 μm laser light out of the fiber into a sample for exciting e.g. Er-doped planar optical waveguides or Er-doped planar structures. This setup is schematically depicted in Fig. 14. The setup is built on an optical table with active, compressed air damped isolators. The table is placed in a flowbox for dust-free operation. The 1.48 μm laser output is coupled out of the fiber by means of a **fiber collimator**, which consists of a FC/PC connector for the connectorized fiber and an achromatic GRIN (graded index) lens optimised for light in the wavelength range of 1300 to 1550 nm. The collimator has setscrews for fine-tuning of the angular position and a C-mount thread for mounting in an optical positioning system. The collimated beam has a diameter of 1.5 mm. A **4x beam expander** consisting of a plano-concave, AR-coated lens (f -25.0 mm) and a plano-convex, AR-coated lens (f +100 mm) at a relative distance of 75 mm results in a 6 mm laser beam. A **beamsplitter** consisting of sodalime glass of 0.3 mm thick reflects approx. 25% and transmits 75% of the laser light and is used for both **pump power measurements** and merging of a small **HeNe laser** beam into the infrared light. The combined beam is focused onto the side of a sample for in-plane coupling of laser light into an **Er-doped film** or **waveguide** on a planar substrate. Since the human eye is not sensitive to the pump laser wavelength, the 633 nm (red) HeNe line is used for visible alignment of the laser beam to the sample edge. Coarse alignment of the sample is performed by eye using the red scattered light and a simple daylight **microscope** (magnification ratio 300x) positioned above the sample.

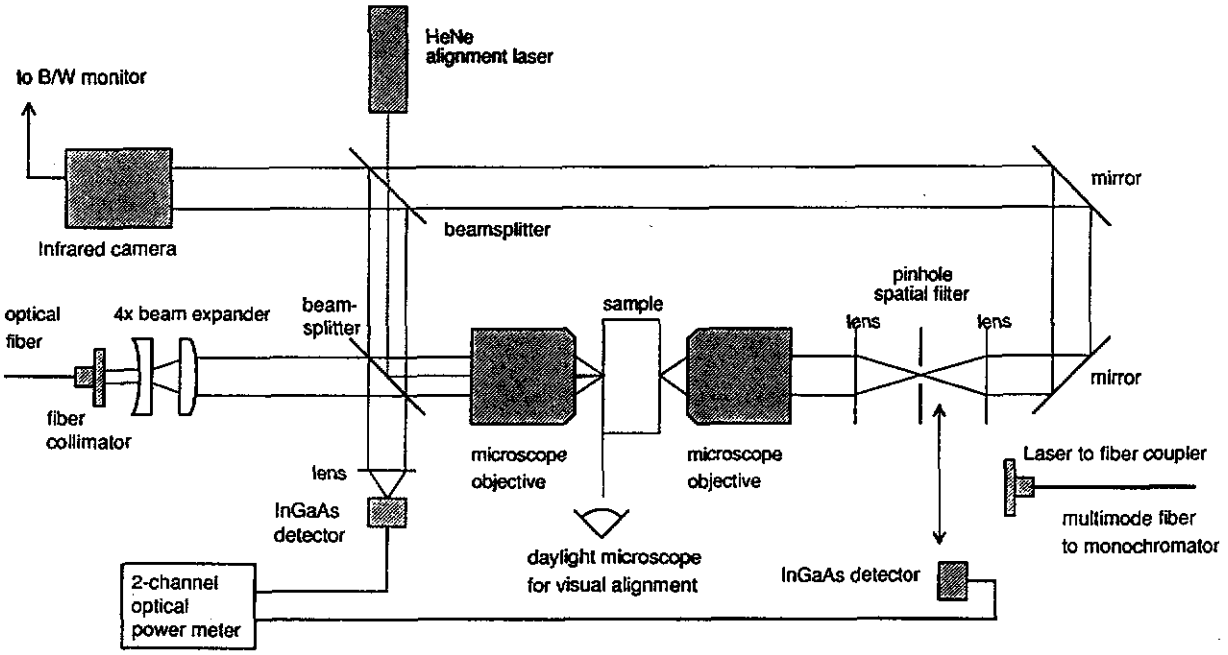

Figure 14: Schematic of experimental setup for high-intensity in-plane coupling of pump laser into Er-doped thin films.

Finetuning can be performed using an **infrared camera** and **B/W video monitor** for visualizing infrared pump light scattered from the polished front face of the sample or coupled out of the end face. A set of mirrors and a 50:50 cube beamsplitter enable inspection of both front and end faces at the same time using only one camera. Furthermore the camera can be used for near-field mode profile measurements on light emerging from a waveguide for qualitative analysis of the optical mode in the guide.

A less elaborate alignment of pump light to sample is possible in Er-doped films which show visible green upconversion light upon high-intensity excitation. The occurrence of this green luminescence indicates coupling into an Er-doped layer and makes visual alignment possible. In most cases the HeNe beam is only necessary for rough alignment of the height and the focal distance of the incoupling microscope objective. Using the green light, the daylight microscope will suffice for precise alignment of the laser to the sample.

The **incoupling microscope objective** is placed on a **nanopositioning XYZ-translational stage** with piezo-electric actuators for stable alignment with a translational resolution of 20 nm. The incoupling microscope objective has to be chosen according to the properties of the sample, analogous to the coupling of laser beam to fiber as discussed in section 2.1. Coupling into a waveguide requires matching of the beam to the NA and field mode diameter in the waveguide, coupling into thin films — without lateral confinement — requires a focal spot of the same magnitude as the thickness of the Er-doped layer. For the experiments on thin Y_2O_3 films on an oxidised Si substrate as described in chapter 4 the 40x objective is used for incoupling. Using (5.4), the (diffraction limited) focal spot size for this microscope objective is found to be 2 μm^2.

The sample is placed on a **waveguide manipulator** providing four degrees of freedom: YZ translations and $\delta Y \delta Z$ rotations. Sample mounts of various lengths are present, including a mount with vacuum ports, pumped by a small membrane pump.

The **outcoupling objective** is placed on a **micropositioning XYZ-translational stage** with an extended platform for accurate approaching of the end face of the sample. The NA of the objective should match the NA of the sample; in general the in- and outcoupling optics are identical.

A serious disadvantage of collecting Er luminescence at the end face of the sample is the dominant presence of laser light propagating through the film. This problem can be reduced by measuring the luminescence normal to the sample, using the fact that Er ions luminesce in all directions whereas the laser light is guided through the high-index Y_2O_3 film. The luminescence emerges from the uncladded film and is collected with a **stripped silica fiber** with a diameter of 0.8 mm. The fiber is suspended from the daylight microscope supporting equipment and collects the light emitted from approx. 1 mm^2 of the sample surface. This 'suspended fiber' method also enables the probing of luminescence at a specific location on the sample. For the luminescence measurements in the experiments as described in chapter 2, the fiber is positioned directly above the spot where the high-intensity laser is coupled in.

The light coupled out of the end face of the sample can be **spatially filtered** by means of two plano-convex lenses (f +75.6 mm) and a pinhole obstructing all the light which did not emerge from the Gaussian mode profile in the sample. Spatial filtering is based on the fact that in the focus of a lens the Fourier transformation of the beam is projected. A Gaussian beam profile will remain Gaussian upon transformation

and end up near the optical axis, but spatial wavelengths smaller than the diameter of the initial beam are projected further off axis.

The optimal pinhole diameter D_{opt} can be found using:[13]

$$D_{opt} = 2\lambda\left(\frac{F}{D}\right) \tag{6.5}$$

where λ is the wavelength of the laser, F and D respectively the focal length and clear aperture of the lens focusing the beam onto the pinhole. This aperture passes 99.3% of the total beam energy and blocks the spatial smaller wavelengths. No diffraction effects will be caused by this aperture. For 1.53 μm light, D_{opt} is 39 μm. In this setup a standard pinhole with a diameter of 50 μm is mounted.

In order to perform spectroscopy on the light that couples out of the sample, the beam can be inserted into a **laser to fiber coupler** connected to a **multimode fiber** (core diameter 100 μm, length 16 m) for transport to a monochromator and infrared or visible detectors. The photoluminescence spectroscopy setup is described in section 2.4.

A dual channel optical power meter can be applied for power measurements at any position in the beam. Two types of sensor heads may be used; InGaAs and Si, sensitive in respectively the 800-1800 nm and the 360-1100 nm wavelength range. The reflection from a beamsplitter is focused onto an InGaAs sensor head and an analogue representation of the measured power or a connection via a GPIB computer interface can be used as a pump power stability check at any experiment employing the laser diode.

Except of the sample holder and the microscope objectives, all optical components are placed in a rigid Mikrobank positioning system with a well-defined optical axis, which combines a precise and stable alignment of the beam with a fast and straighforward positioning of filters, beamstops, lenses and mirrors.

7. Appendix B

7.1 Instructions for optical coupling of laser diode to fiber

This checklist describes a complete alignment sequence of laser diode to fiber. The instructions at 3, 5, 6 and 7 are only needed when the laser diode is misaligned. During normal operation the position of the laser diode can be left untouched and only fine-tuning of the fiber tip position is performed.

1. Switch on the laser diode controller.
2. Activate the thermoelectric cooling (Peltier element) of the diode heatsink. Make sure the temperature setting is correct.
3. Check whether the laser diode holder is properly attached to the platform of the leftmost Microblock.
4. Switch on the laser. An infrared sensitive card can be used to locate the beam. The high intensity laser output is invisible but very hazardous to eye tissue when collimated and focused! **Before alignment of the laser to the fiber a warming up period of 45 minutes must be taken into account.**
5. Attach the 40x objective (or another appropriate microscope objective for collecting the laser light) to an objective mount. Do not insert a focusing objective. Attach the mount to the shallow fixed platform. Adjust the working distance between laser and lens; 0.4 mm for the 40x lens.
6. The infrared beam can be made visible with an infrared sensitive card. Use this card to optimise the position of the laser. The beam emerging from the microscope objective must be collimated and aligned with the optical axis of the microscope objective mount (75 mm above the breadboard). The Microblock has differential micrometers for coarse and fine translational adjustments. Do not dig the diode into the objective!
7. Carefully attach the 4x objective (or another microscope objective for focusing of the beam) to the open end of the objective mount. Mount the fiber holder on the platform of the rightmost Microblock. Use the infrared card for rough alignment of the fiber tip to the laser spot.
8. Monitor the laser power at the other end of the fiber by means of an infrared detector and an optical power meter.
9. Align the fiber tip with the laser spot (use filters to prevent overloading of the power meter; max. 1.5 mW on detector) and optimise the working distance between the laser diode and the collecting microscope objective. The coupling should be stable within 10 mW during a day. However, the micrometers do show some creep and sticking. Only the position of the fiber has to be kept optimised once in a while. The alignment of the diode is left untouched.

References

1 R.W.C. Wyckoff,*Crystal structures, volume 2*, (Interscience, New York, 2nd ed. 1964)

2 T.H. Hoekstra, P.V. Lambeck, H. Albers and Th.J.A. Popma, Electron. Lett.**29** 581 (1993)

3 A. Polman, A.M. Vredenberg, W.H. Urbanus, P.J. van Deenen, H. Alberda, H. Krop, I. Attema, E. de Haas, H. Kersten, S. Doorn, J. Derks, J. ter Beek, S. Roorda, R. Schreutelkamp, J.G. Bannenburg and F.W.Saris, Nucl. Instr. and Meth. **B37/38** 935 (1989)

4 J.P. Biersack and L.J. Haggmark, Nucl. Instr. and Meth.**174** (1980)

5 L.R. Doolittle, Nucl. Instr.and Meth. **B9** 334 (1985)

6 T.H. Hoekstra, Ph.D. Thesis, Lightwave Devices Group, MESA Research Institute, University of Twente, 1994

7 W.F. Krupke, Phys. Rev.**145**, 325 (1966)

8 R.S. Quimby, W.J. Miniscalco and B. Thompson, submitted to SPIE OE/Fibers, 1992

9 P. Blixt, J. Nilsson, T. Carläs and B. Jaskorzynska, IEEE Photon. Technol. Lett. **3** 996 (1991)

10 J. Thøgerson, N. Bjerre and J. Mark, Opt. Lett. **18**, 197 (1993)

11 G.H. Dieke, in *Spectra and Energy levels of rare earth ions in crystals*, ed. by H.M. Crosswhite and H. Crosswhite, (Interscience publishers, New York, 1968)

12 A.W. Snyder, Proc. IEEE, Jan. 1981, Vol.1, 6-13

13 Newport Catalog 1993, Optics Reference Guide